Shock Waves (2010) 20:103–118
DOI 10.1007/s00193-010-0247-1

ORIGINAL ARTICLE

Numerical and experimental investigation of transverse injection flows

E. Erdem · K. Kontis

Received: 3 December 2008 / Revised: 19 January 2010 / Accepted: 24 January 2010 / Published online: 24 February 2010

Abstract The flow field resulting from a transverse injection through a slot into supersonic flow is numerically simulated by solving Favre-averaged Navier–Stokes equations with $\kappa - \omega$ SST turbulence model with corrections for compressibility and transition. Numerical results are compared to experimental data in terms of surface pressure profiles, boundary layer separation location, transition location, and flow structures at the upstream and downstream of the jet. Results show good agreement with experimental data for a wide range of pressure ratios and transition locations are captured with acceptable accuracy. $\kappa - \omega$ SST model provides quite accurate results for such a complex flow field. Moreover, few experiments involving a sonic round jet injected on a flat plate into high-speed crossflow at Mach 5 are carried out. These experiments are three-dimensional in nature. The effect of pressure ratio on three-dimensional jet interaction dynamics is sought. Jet penetration is found to be a non-linear function of jet to free stream momentum flux ratio.

Keywords Flows and jets through nozzles · Supersonic flows · CFD

1 Introduction

Transverse injection into a supersonic crossflow has been encountered in many engineering applications ranging from scramjet combustors and solid rocket motor or liquid engine thrust vector control systems to high-speed flight vehicle reaction control jets. Efficient combustion via mixing enhancement is the goal in scramjet fuel injection systems, whereas in thrust vector control systems and reaction control jet applications the objective is to divert the main flow in order to gain additional side forces. These applications all involve complex three-dimensional flow patterns comprising separated regions, shock waves, shear layers and wakes. Owing to these complicated flow features, transverse injections over flat plates and various forebodies have been receiving significant amount of interest for years. Earlier studies were focused on wind tunnel tests with conventional measurement techniques such as schlieren/shadowgraph photography and wall pressure measurements. Spaid and Zukoski [1] investigated sonic slot jet injection on a flat plate at three different Mach and Reynolds numbers, and various injection pressures of different gases like N_2 and He; afterwards, Spaid [2] expanded this study by injecting through a round orifice on a flat plate at a broader range of Mach and Reynolds numbers. Schetz and Billig [3] conducted more or less the same study with a round jet on a flat plate at a specific supersonic Mach number, Parthasarathy and Zakkay [4] examined the effect of slot injection on a streamlined centre body at hypersonic speeds, Hawk and Amick [5] experimented slot injection on a wedge of rectangular platform and so did Werle et al. [6] on a flat plate. Papamoschou [7] visually observed round sonic and supersonic He jets normal to a supersonic crossflow. Recently, Kumar et al. [8] and Kontis and Stollery [9] investigated the control effectiveness of a jet issuing over a slender body in terms of aerodynamic performance and stability in hypersonic regime. In essence, all these studies aimed to assess the effect of injection pressure ratio, location of injection and state of incoming boundary layer and type of injectant gas on supersonic jet interaction phenomenon, whether it is for thrust vectoring or scramjet combustion.

On the other hand, Computational Fluid Dynamics (CFD) has been utilised for these type of interactions since 1990s.

Communicated by E. V. Timofeev.

E. Erdem (✉) · K. Kontis
School of MACE, The University of Manchester, Manchester, UK
e-mail: erinc.erdem@postgrad.manchester.ac.uk

Due to complex flow features occurring simultaneously, transverse jet injection flows have served as good candidate to validate and test the performance of turbulence models ranging from Reynolds Averaged Navier–Stokes (RANS) models to Detached Eddy Simulation (DES) models. Earlier attempts started by Rizetta [10], who solved two-dimensional Navier–Stokes equations on a flat plate with slot injection over a range of slot widths and slot total pressure ratios. Low Reynolds number $\kappa - \epsilon$ model with compressibility correction was applied. Results show considerable disagreement between numerical and the experimental data in terms of wall pressure distributions and the extent of the separation region. The primary cause for disagreement was believed to come from three-dimensional effects in the experiment and the compressibility correction applied. Dhinagaran and Bose [11] employed Baldwin–Lomax algebraic turbulence model to simulate the two-dimensional experimental case of Spaid and Zukoski [1]. They paid extra attention to capture transitional separation at the highest Mach number case; results suggested poor agreement for the cases with turbulent separation, especially at high pressure ratios; however, for the cases with transitional separation agreement was satisfactory. Chenault and Beran [12] studied the effect of turbulence models such as $\kappa - \epsilon$ model with a compressibility correction and Reynolds Stress Model (RSM). As an experimental data set, authors emphasised the use of data from Spaid and Zukoski [1] for proper comparison. Results showed very good agreement at low- and moderate pressure ratios; however, as the jet pressure ratio was increased the computed wall pressure distributions started to differ at the upstream region and the injection port vicinity. The discrepancies were addressed to the lack of knowledge of incoming turbulent conditions at the nozzle exit during wind tunnel tests. The superiority of RSM over $\kappa - \epsilon$ model was recognized at Reynolds stress profiles; the inconsistency in vorticity values for $\kappa - \epsilon$ model was associated with the evaluation of wall functions under adverse pressure gradients. Qin and Redlich [13] examined the case of a laminar separation due to a slot jet injection over a flat plate and compared the results with experimental data. The agreement was satisfactory in terms of wall pressure distribution, yet not perfect implying complex character of the flow field to model even in the absence of a turbulence model. Recently, Srinivasan and Bowersox [14] assessed the performance of $\kappa - \omega$ SST and DES models for two- and three-dimensional sonic/supersonic injection flows with different injectors by solving three-dimensional Navier–Stokes equations. Results revealed no significant discrepancies between models when compared with experimental data except for the resolution of unsteady vortical flow structures where DES performed better. Won et al. [15] compared $\kappa - \omega$ SST and DES models as well for the case of Spaid and Zukoski [1]; the agreement was found to be satisfactory at low- and moderate jet pressure ratios; nevertheless, computed pressure

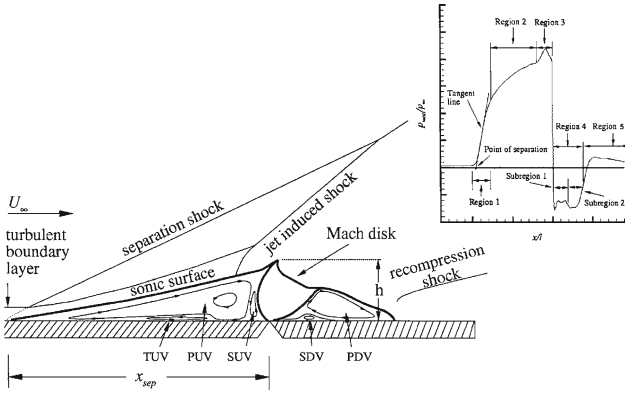

Fig. 1 Two-dimensional transverse slot injection flow field features by Chenault and Beran [12]

distributions showed disparities at high pressure ratios at the upstream separation region and the injection port neighbourhood. DES model generally overpredicted mean flow properties compared with SST model. Sriram and Mathew [16] solved two-dimensional flow field with $\kappa - \omega$ SST model for the case of Spaid and Zukoski [1]. They improved their early results basically by refining the computational grid over the boundary layer up to Mach disc (see Fig. 1), yet wall pressure levels were still overpredicted at high pressure ratios.

The present investigation attempts to improve numerical simulations to match experimental data of Spaid and Zukoski [1] for a wider range of pressure ratios, including capturing transition locations mentioned in experiments, and to investigate the effect of incoming flow and jet turbulence levels on jet interaction phenomenon. To compliment numerical simulations, few experiments involving a sonic round jet injected on a flat plate into high-speed crossflow at Mach 5 are carried out. These experiments are three-dimensional in nature. The effect of pressure ratio on jet interaction dynamics is sought.

The flow features of transverse slot injection over a flat plate in supersonic crossflow are shown in Fig. 1. The secondary jet basically acts as an obstruction on the main flow, diverting it to move above the injection plume. This blockage projects itself by a strong jet-induced bow shock upstream in the inviscid region. Consequently, due to the presence of this bow shock an adverse pressure gradient is imposed on the incoming turbulent boundary layer, causing it to separate upstream. The flow structure in the turbulent boundary layer involves two counter-rotating vortices, primary upstream vortex (PUV) and secondary upstream vortex (SUV). The boundary layer displacement of these vortices causes a weak separation shock that interacts with the strong bow shock. In between the recirculation region and separation shock there is a sonic surface which essentially displaces the incoming flow. On the injection port the under expanded sonic transverse jet suddenly accelerates and expands into the main flow and results in reduced pressures. This expansion is ended by

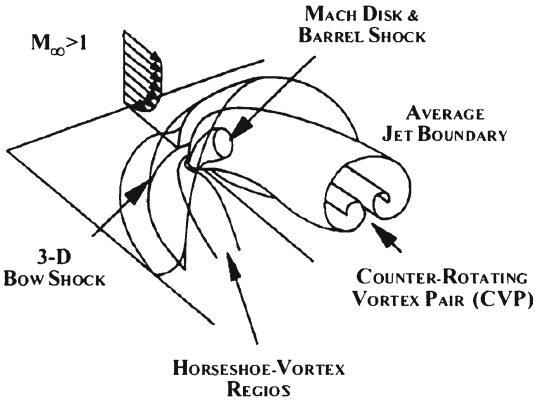

Fig. 2 Three-dimensional perspective of the averaged features of the flow field by Gruber et al. [17]

a normal shock; resulting in a Mach surface surrounding the jet plume. Finally, at the downstream of the injection location the diverted main flow is turned parallel to the nozzle wall via a recompression shock accompanied by a recirculation region forming primary and secondary downstream vortices (PDV and SDV). In two-dimensional configurations a third upstream vortex (TUV) might occur occasionally.

In the wall static pressure profile (Fig. 1) there are five distinct regions reported by Chenault and Beran [12]; an upstream region of steep pressure rise (region 1) as a result of boundary layer separation, then a flattening of the pressure upstream of the jet (region 2) caused by PUV. The pressure plateau is followed by a pressure spike (region 3) caused by the SUV. Immediately downstream of the jet is a large pressure drop (region 4) with two subregions. The first subregion is a slight pressure rise caused by the leading edge of the PDV. The second subregion is a pressure drop caused by the SDV. The pressure drop is followed by a pressure hump (region 5) associated with the trailing edge of the PDV, boundary layer reattachment, and the recompression shock.

In case of a transverse injection through a single circular hole into a crossflow, significant fluid motion in spanwise direction is observed as opposed to two-dimensional case. First two counter-rotating vortices, emerging on top of Mach disc and a horseshoe vortex, formed by the SUV, propagate downstream; second the separation shock and the bow shock are curved and extended in spanwise direction. Incoming flow is diverted both above and on the sides of the injection port as shown in Fig. 2 as depicted by Gruber et al, Santiago and Dutton, Chenault et al., and Srinivasan and Bowersox [17–20]. The pair of counter-rotating crossflow vortices is assessed by Gruber et al. [17] as the primary source of entrainment of the surrounding incoming flow air into the injectant's stream which is important for far field mixing. The horseshoe vortices wrap around the upstream side of the jet and trail downstream, and wake vortices, formed by PDV, periodically shed near the base of the inner jet core. Thus, the three-dimensional relieving effect assists incoming flow to move around the transverse jet, which reduces the maximum value of the surface static pressure, and it causes upstream separation point move closer to the jet. Moreover, downstream recompression is curved and extended in spanwise direction as well.

2 Experimental data description for slot jet injection

In the experimental data set of Spaid and Zukoski [1], jet was injected through a converging slot of 0.2667 mm wide across the spanwise direction at a station of 228.6 mm from the leading edge of the plate. The injectant gases were N_2 and He. A series of free stream Mach and unit Reynolds numbers were tested from 2.61 and 11.48×10^6 1/m, 3.5 and 13.12×10^6 1/m, 4.54 and 12.8×10^6 1/m, respectively. The measured quantities were reservoir conditions for both free stream and the jet and wall pressures on the flat plate. It is a commonly used test case for under expanded injection flows into supersonic crossflows due to its coverage of a wide range of jet to free stream pressure ratios (p_{jet}/p_∞) from 8.79 to 63.61 and jet to free stream momentum flux ratios ($J = \gamma_{\text{jet}} p_{\text{jet}} M_{\text{jet}}^2 / \gamma_\infty p_\infty M_\infty^2$) from 0.72 to 6.77 in a well-documented systematic way. Precaution was taken to ensure two-dimensionality by the use of side plates; three-dimensional complications were reported as separation region extends to the forward of side plates, especially at highest Mach number case. Extensive amount of pressure tappings was used and nicely spread providing good spatial accuracy and gradually changing wall pressure plots. Boundary layer was tripped at the leading edge by a trip wire, but transition was reported to occur 50.8–76.2 mm from the leading edge by shadowgraph photography for M_∞ of 2.61 and 3.50. At M_∞ of 4.54 the interaction between jet and the crossflow was reported to be transitional based on wall pressure distribution and shadowgraph images; moreover, the loss of two-dimensionality was mentioned. Among different cases, following ones are chosen for comparison in this study as shown in Table 1: the pressure variation on the wall in conjunction with the flow structures around the injection slot is drawn in Fig. 3. M_1 and p_1 are the upstream Mach number and pressure, respectively, just at the upstream of separated region outside of the boundary layer, whereas p_2 is the plateau pressure at the downstream of separation shock, at the edge of shear layer. The data were presented in terms of p/p_1 against distance from the leading edge of the flat plate, not in terms of p/p_∞. The reason for that might have been the need to assess the jet interaction phenomenon with respect to undisturbed boundary layer flow developed on the flat plate rather than with respect to freestream conditions. One important thing to note is that p_1 is greater than p_∞ due to the leading edge shock wave which is associated with the phenomenon called

Table 1 Flow conditions by Spaid and Zukoski [1]

Case	p_0 (bar)	T_0 (K)	$p_{0\text{jet}}$ (bar)	$T_{0\text{jet}}$ (K)
1	1.34	318	1.59	298
2	1.32	318	3.00	294
3	1.33	318	5.73	291
4	2.40	309	0.52	292
5	2.41	311	1.02	293
6	2.41	313	1.94	293
7	2.41	314	3.80	292

For cases 1–3
$M_\infty = 2.61$ and $Re/m = 11.48 \times 10^6 (1/m)$
$p_{0\text{jet}}/p_1 = 23.5$, 44.5 and 82.9
$J = 1.87$, 3.57 and 6.77
For cases 4–7
$M_\infty = 3.50$ and $Re/m = 13.12 \times 10^6 (1/m)$
$p_{0jet}/p_1 = 16.55$, 32.4, 61.3 and 120.2
$J = 0.72$, 1.4, 2.65 and 5.19

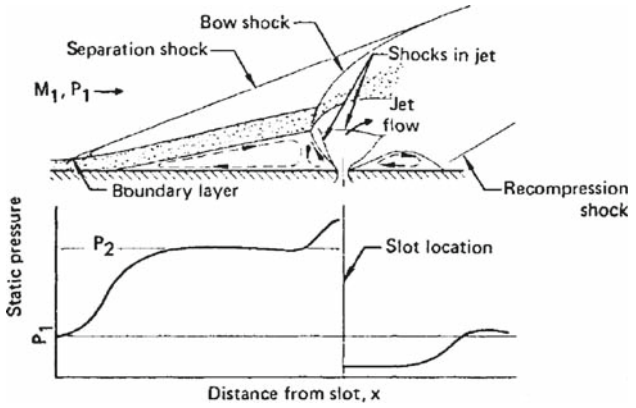

Fig. 3 Two-dimensional transverse slot injection nomenclature by Spaid and Zukoski [1]

'viscous interaction' peculiar to high-speed flat plate flows. Due to the sudden increase of boundary layer thickness and hence displacement thickness on the surface, outer inviscid flow sees an effectively thicker body with growing thickness. In return it has to go through a smaller streamtube area and has to change its direction. This occurs with a curved shock wave forming at the leading edge. As a consequence, the outer flow at the edge of boundary layer is altered and pressure levels are increased.

3 Numerical method

3.1 Numerical solver

In the current study, Favre-Averaged Navier–Stokes (FANS) equations are solved with density based (coupled) double precision solver of FLUENT®. Second order spatially accurate upwind scheme (SOU) with Roe's Flux-Difference Splitting

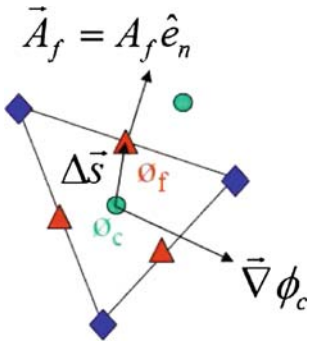

Fig. 4 Cell nomenclature

is utilised. In this scheme formulation second-order accuracy is achieved at cell faces through a Taylor series expansion of the cell-centred solution about the cell centroid. Therefore, the face value of a flow variable, ϕ_f is computed using the following equation [21]:

$$\phi_{\text{f,SOU}} = \phi_\text{c} + \nabla\phi_\text{c} \cdot \Delta\mathbf{s} \tag{1}$$

where ϕ and $\nabla\phi$ are the cell-centred value and its gradient in the upstream cell, and $\Delta\mathbf{s}$ is the displacement vector from the upstream cell centroid to the face centroid as shown clearly in Fig. 4.

This formulation requires the determination of the gradient in each cell centre. For this purpose, $\nabla\phi_\text{c}$ is expressed as a summation of values at the cell faces using Green–Gauss theorem shown below.

$$\nabla\phi_\text{c} = \frac{1}{\mathcal{V}} \sum_\text{f} \overline{\phi}_\text{f}\, \mathbf{A}_\text{f} \tag{2}$$

where ϕ_f is the value of ϕ at the cell face centroid. Consequently for the evaluation of face values, the arithmetic average of the nodal values on the face is computed as expressed in (3).

$$\overline{\phi}_\text{f} = \frac{1}{N_\text{f}} \sum_{n}^{N_\text{f}} \overline{\phi}_\text{n} \tag{3}$$

where N_f is the number of nodes on the face. The nodal values, $\overline{\phi}_\text{n}$ are constructed from the weighted average of the cell values surrounding the nodes in an unstructured manner as shown below in Fig. 5. In structured meshes the weighted average is the average of four cells surrounding the node in two dimensions.

Finally, the gradient of ϕ is limited with ψ in the second term of (4) so that no spurious wiggles are introduced; the limiter adapted is the one from Venkatakrishnan [21]. It is based on a comparison of the actual ϕ value at the adjacent cell, c1, with the one estimated by evaluating $\nabla\phi_\text{c}$ and $\Delta\mathbf{s}_{0-1}$ at c0 (see Fig. 5) using (1). If the estimated value is much larger in magnitude, an extremum is detected and the gradient is limited by a scale factor.

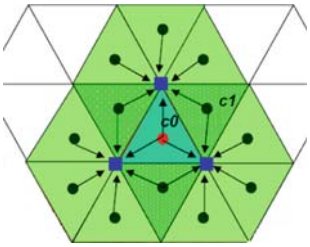

Fig. 5 Green–Gauss node-based gradient evaluation stencil

$$\phi_f = \phi_c + \psi \nabla \phi_c \cdot \Delta \mathbf{s} \tag{4}$$

3.2 Turbulence model and solver parameters

In case of the turbulence model, Shear-Stress Transport (SST) $\kappa - \omega$ model of Menter is adapted as it was suggested by Srinivasan and Bowersox [14], Won et al. [15], and Sriram and Mathew [16] and found to be accurate, especially for boundary layer flows in the presence of adverse pressure gradients in user documentation [21]. In this model, $\kappa - \omega$ at near-wall region is blended with $\kappa - \epsilon$ outside boundary layer. The transport equations for κ and ω are specified below in (5) and (6). Moreover, the corrections for compressibility and transition are applied. The correction for transition is nothing but a low Reynolds number modification to the turbulent viscosity.

$$\frac{\partial}{\partial t}(\rho k) + \frac{\partial}{\partial x_i}(\rho k u_i) = \frac{\partial}{\partial x_j}\left(\Gamma_k \frac{\partial k}{\partial x_j}\right) + \tilde{G}_k - Y_k + S_k \tag{5}$$

and

$$\frac{\partial}{\partial t}(\rho \omega) + \frac{\partial}{\partial x_i}(\rho \omega u_i) = \frac{\partial}{\partial x_j}\left(\Gamma_\omega \frac{\partial \omega}{\partial x_j}\right) + G_\omega - Y_\omega + D_\omega + S_\omega \tag{6}$$

In case of compressibility correction, compressibility affects turbulence through the so-called "dilatation dissipation", which accounts for the decrease in spreading or growing rate of mixing layers or free shear layers with increasing convective Mach number that is well documented by Smits and Dussage [22]. Specifically for this model, compressibility takes part in dissipation terms such as Y_k and Y_ω and partially in the production of turbulence kinetic energy as defined below.

$$Y_k = \rho \beta^* k \omega \quad \text{and} \quad Y_\omega = \rho \beta \omega^2$$

where β^* and β are expressed below as functions of $F(M_t)$:

$$\beta^* = \beta_i^* \left[1 + \zeta^* F(M_t)\right] \tag{7}$$

$$\beta = \beta_i \left[1 - \frac{\beta_i^*}{\beta_i} \zeta^* F(M_t)\right] \tag{8}$$

$\zeta^* = 1.5$ and other parameters are defined in user documentation [21]. The compressibility function, $F(M_t)$, is given by following conditional expression:

$$F(M_t) = \begin{cases} 0 & M_t \le M_{t_0} \\ M_t^2 - M_{t_0}^2 & M_t > M_{t_0} \end{cases}$$

where

$$M_t^2 = \frac{2k}{a^2} \qquad M_{t_0} = 0.25 \qquad a = \sqrt{\gamma RT}$$

Last, the term $\tilde{G}_k$ represents the production of turbulence kinetic energy which involves β^*, and is affected by compressibility as well, as shown below.

$$\tilde{G}_k = \min(G_k, 10\rho\beta^* k\omega)$$

where G_k is defined in the same manner as in the standard $\kappa - \omega$ model as with other constants [21].

In case of solver parameters Courant–Friedrichs–Levy (CFL) condition is kept at 0.5 with proper under-relaxation factors to ensure stability. Full-multi grid initialization technique that solves Euler equations at a certain number of temporary grid levels starting from coarse to fine and then sets the fine grid level solution as an initial solution, is employed rather than providing constant initial conditions to start simulation with. The benefit of this technique is accelerated convergence.

3.3 Computational grid and boundary conditions

The computational domain is simply a rectangle surrounded by adiabatic walls at the bottom, supersonic inlet at the left boundary and sonic inlet at the injection port, an outlet at the right boundary and finally a far-field boundary on top. Moreover, the domain is extended both upstream and downstream directions to ensure that boundary conditions are physically reasonable so that simulation converges healthily. The extended upstream region of 10 mm in front of the plate is set as symmetry as a boundary condition. The size of the computational domain is set to 365.6 mm × 100 mm.

Five computational grids that are made of quadrilateral cells of 312 × 190, 397 × 190, 482 × 190, 482 × 150 and 482 × 260 are generated. The grid density is clustered towards the injection port for all grids and relaxed towards outlet. A boundary layer grid is generated on the bottom wall with a first cell height of 0.01 mm. This boundary layer grid is in fact extended well over the actual boundary layer up to 27 mm from the wall normal in order to better resolve circulating and interacting flow structures close to injection port as suggested by Sriram and Mathew [16]. In the symmetry region, 12 grid points are assigned in a stretching manner towards the leading edge and leading edge grid density is clustered as well to better treat leading edge shock due to

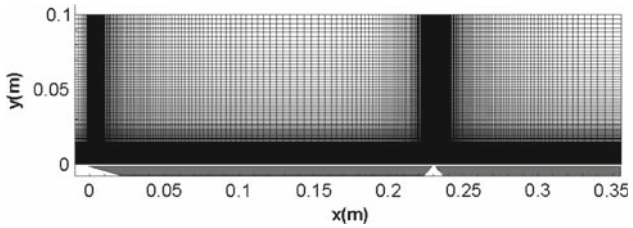

Fig. 6 Computational grid

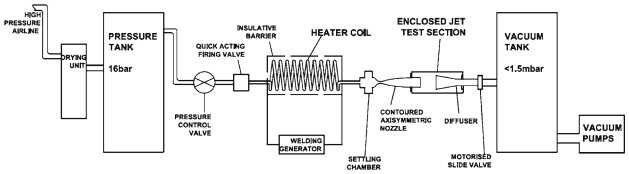

Fig. 7 University of Manchester HSST schematic layout

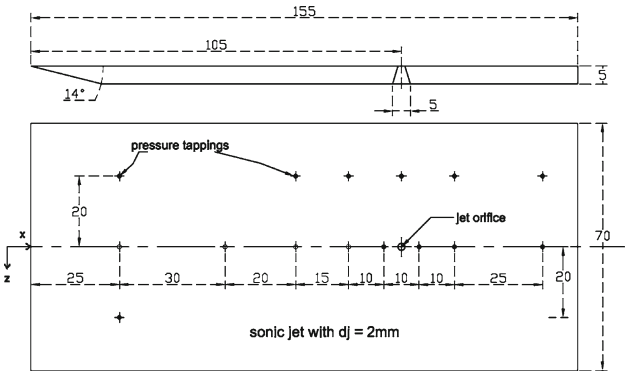

Fig. 8 Flat plate model for jet interaction study, all in mm

viscous interaction. The computational domain with grid is shown in Fig. 6.

Air is assumed to be a thermally and calorically perfect gas; Sutherland's law of viscosity is employed. At the supersonic inflow, uniform stagnation conditions (p_0 and T_0) and static pressure (p) are specified together (see Table 1). For turbulence quantities, different turbulent intensity (TI) levels are tested such as 0.005, 0.05, 0.5, 5 and 10% due to the fact that inflow turbulent quantities were not specified in the experimental data set, and turbulent (eddy) viscosity is set to fluid viscosity. At the jet orifice sonic conditions are simply prescribed. In addition, a set of jet TI values of 0.5, 2.5 and 5% are tested to investigate the effect of jet turbulence due to the aforementioned reason, and hydraulic diameter (D_h) is assigned to a value that is two times the width of the slot for two-dimensional injection. Furthermore, κ and ω values of 100 m^2/s^2 and $5 \times 10^5 s^{-1}$, respectively, that are proposed by Sriram and Mathew [16] are tested for comparison.

4 Experimental method for round jet injection

4.1 Experimental facility

The experiments are conducted in the High Supersonic Tunnel (HSST) of the University of Manchester. The tunnel is an intermediate blowdown (pressure–vacuum) type which uses dry air as working fluid and shown schematically in Fig. 7. Air from high-pressure airline is dried and stored in a pressure vessel at 16 bar. After passing through a pneumatically operated quick-acting ball valve, the gas enters the electric resistive heater. The gas temperature is raised from ambient to temperature between that sufficient to avoid liquefaction on its expansion through the nozzle and that of a maximum enthalpy flow condition of 700 K. On leaving the heater air enters the settling chamber which is downstream of the flow straightener matrix. Immediately downstream of the settling chamber is situated a contoured axisymmetric Mach 5 nozzle. The stagnation pressure can be ranged from 6 to 8 bar and thereby unit Reynolds numbers, Re/m, of between $4.5 - 15 \times 10^6$1/m can be achieved. The tunnel working section is an enclosed free jet design. The calibration of the facility was carried out by the authors; the variations in Mach number and unit Reynolds number were found to be ± 0.4 and $\pm 3\%$, respectively.

4.2 Experimental model

The model used for this study is a sharp leading edge flat plate with a converging jet hole, through which a sonic turbulent jet is injected after regulation. The flat plate is shown below in Fig. 8.

4.3 Flow diagnostics

Stagnation pressure and temperature measurements are done using a pitot probe attached to an absolute pressure transducer, Kulite XTE-190M (0–6.895 bar), and a K-type thermocouple probe at the settling chamber, whereas wall pressure and jet stagnation pressure measurements are carried out using absolute pressure transducers Kulite XTE-190M (0–3.5 bar) in the test section. These transducers have an estimated error of $\pm 3\%$. Analog signals from the sensors are acquired by a high-speed Data Acquisition (DAQ) card, National Instruments(NI) PCI-6251, after they are conditioned by a SXCI-1000 unit. The existing system has the capability of collecting data at a frequency up to 333 kHz at 16 bit digitisation. The DAQ has a fully programmable environment; it can generate proper digital or analog signals at a precise time by means of software, LABVIEW v.8.5.

Toepler's z-type schlieren technique is adapted for flow visualisation that consist of a continuous light source of Palflash 501 (Pulse Photonics) with a focusing lens and a 2 mm-wide slit, two 203.2 mm parabolic mirrors with 1.83 m

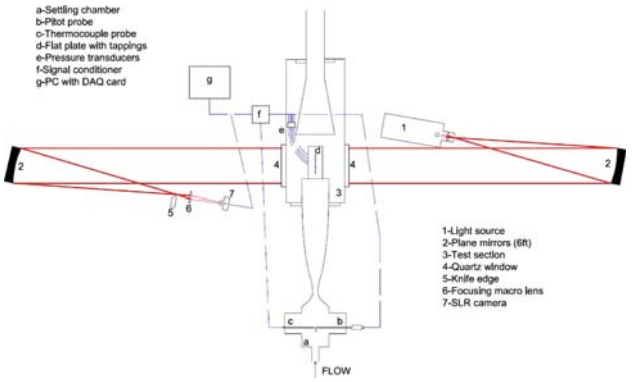

Fig. 9 Schematic setup of schlieren visualisation with DAQ architecture

focal length, a knife edge, a set of Hoya 49 mm close-up lenses and a digital Canon SLR camera, EOS-450D, 12 MP. The offset angle of parabolic mirrors with respect to their axis is set to 3° to prevent optical aberrations such as coma and astigmatism as much as possible. Parallel beam of light is passed through test section windows before focusing on the knife edge plane that is placed parallel to flow direction and the focused beam is shone on CMOS sensor of the camera. The camera is set to continuous shooting mode at which it can record 3.5 fps at full resolution; the shutter speed is adjusted to maximum value of 1/4,000 s with an ISO speed of 400 to provide enough detail and appropriate brightness. The operation of the camera is initiated using 5V TTL trigger signal coming from pressure transducer at the settling chamber. The layout of the optical setup and the DAQ architecture with measurement chain is shown in Fig. 9.

5 Results

5.1 Numerical results-Spaid and Zukoski case

5.1.1 Grid sensitivity and the effects of inlet and jet turbulence levels

Case 7 from Table 1 is selected as the test case (the one with highest po_{jet}/p_1 ratio) to critically assess grid requirements and to study the effect of inlet and injection turbulence levels on results. For the incoming turbulent boundary layer developing on the flat plate at the upstream of the separated region, the definitions of boundary layer, displacement and momentum thicknesses with shape factor are expressed below, and computed using eighth-order polynomial fits. Their values are shown in Table 2. u_e and ρ_e are velocity and density at the boundary layer edge, respectively.

$$\delta = y|_{u=0.99u_e} \tag{9}$$

Table 2 M_1 and p_1 values with boundary layer properties for Case 7

M_1	p_1 (mbar)	δ (mm)	δ^* (mm)	θ (mm)	$H = \delta^*/\theta$
3.48	32.5	2.28	1.09	0.47	2.34

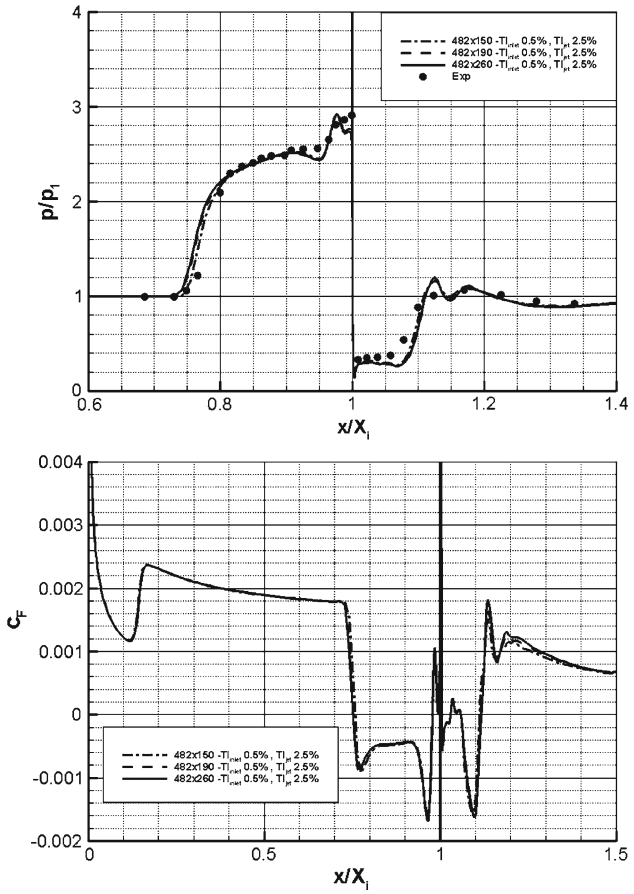

Fig. 10 Non-dimensional pressure (*top*) and skin friction coefficient (*bottom*) distributions at the wall for successive grid refinement in y direction

$$\delta^* = \int_0^\delta \left(1 - \frac{\rho u}{\rho_e u_e}\right) \mathrm{d}y \tag{10}$$

$$\theta = \int_0^\delta \frac{\rho}{\rho_e}\frac{u}{u_e}\left(1 - \frac{\rho u}{\rho_e u_e}\right) \mathrm{d}y \tag{11}$$

$$H = \frac{\delta^*}{\theta} \tag{12}$$

Figures 10 and 11 show the comparison of computed non-dimensional wall pressure distributions (p/p_1) with experimental data and the skin friction coefficient ($c_f = 2\tau_w/\rho_\infty u_\infty^2$) plots for five computational grids with moderate TI level. The horizontal axis is non-dimensionalized by injection location, X_i. All grids captured upstream and downstream prominent flow features; the agreement with the

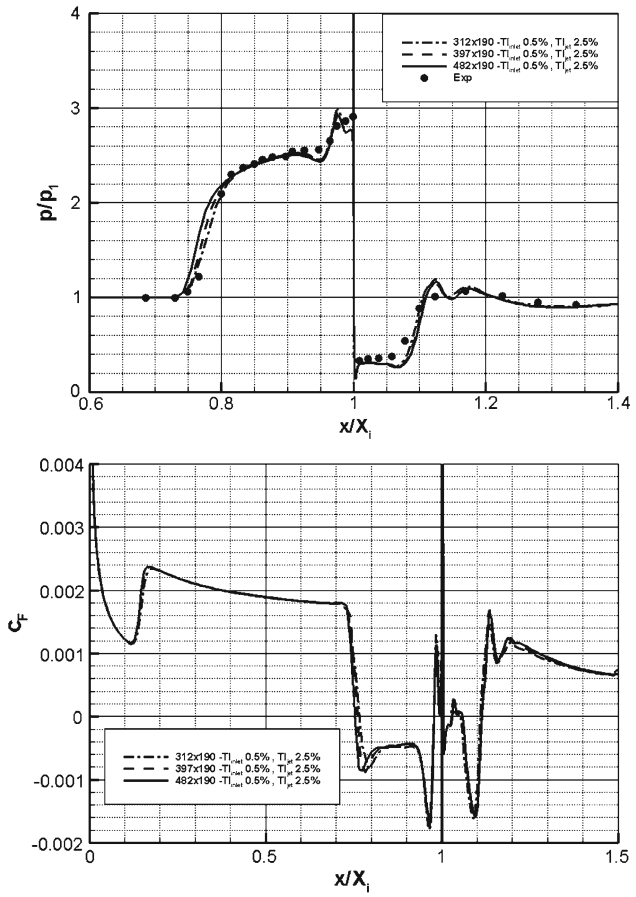

Fig. 11 Non-dimensional pressure (*top*) and skin friction coefficient (*bottom*) distributions at the wall for successive grid refinement in x direction

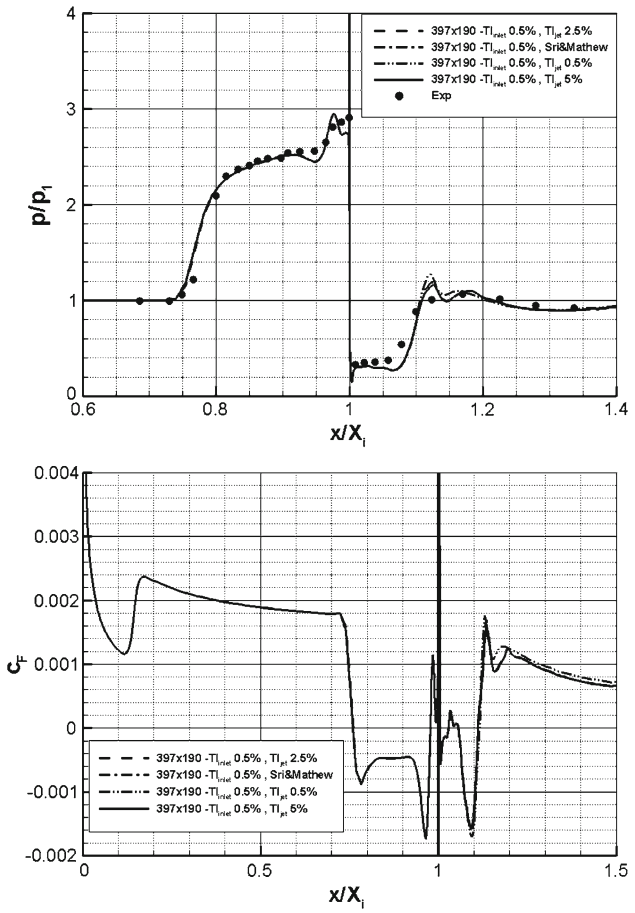

Fig. 12 Non-dimensional pressure (*top*) and skin friction coefficient (*bottom*) distributions at the wall for different jet turbulence intensities

experimental data is good. Nevertheless, computations slightly overpredict the extent of upstream separation region (region 1) and the downstream pressure well (region 4). From Fig. 10 it can be observed that the difference between 482 × 190 and 482 × 260 is insignificant in terms of wall pressure distribution and skin friction coefficient. Only the coarse grid, 482 × 150, deviates from the solution with the finest grid in the upstream and downstream regions; thus the number of grid points in y direction is selected as 190. In case of grid resolution in x direction, 397 grid points are enough to obtain a grid-independent solution as shown from Fig. 11. Hence, numerical solution turned out to be grid-independent beyond a computational grid of 397 × 190. For this grid, wall $y^+(= yu_\tau/\nu)$ values less than 0.5 for almost everywhere in the upstream and downstream regions and a maximum of 2.5 at upstream injection port vicinity are obtained, suggesting compatibility of this grid with a low Reynolds number turbulence model. The expressions for friction velocity and wall shear stress are defined below for completeness.

$$u_\tau = \sqrt{\tau_w/\rho} \quad \text{and} \quad \tau_w = \mu \left(\frac{\partial u}{\partial y}\right)_w$$

Figure 12 shows the comparison of computed non-dimensional wall pressure distribution with experimental data and the skin friction coefficient plot for four injection turbulence intensities with a computational grid of 397 × 190. Jet TI values of 0.5, 2.5 and 5% are tested with propsed κ and ω values of 100 m^2/s^2 and 5×10^5 s^{-1}, respectively. It can be clearly deducted that the results are independent of the jet turbulence. Only small deviation in the downstream pressure hump (region 5) is observed with TI of 0.5%. Therefore a TI of 2.5% is selected as the jet turbulence intensity.

Figure 13 shows the comparison of computed non-dimensional wall pressure distribution with experimental data and the skin friction coefficient plot for five inlet turbulence intensities with a computational grid of 397 × 190. There is not any discernible difference between different inlet turbulence levels in terms of wall pressure distribution; however, transition location is found to be dependent on incoming flow turbulence. In the experimental data description, transition was reported to take place at 50.8–76.2 mm from the leading edge. Moderate turbulence levels such as 5 and 10% result quite early transition, whereas for 0.5% of TI transition occurs

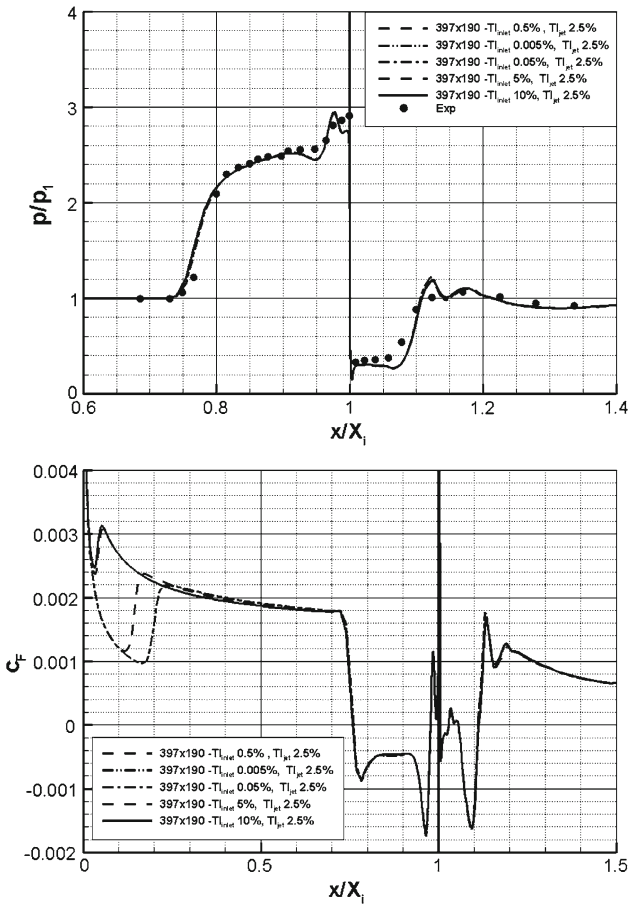

Fig. 13 Non-dimensional pressure (*top*) and skin friction coefficient (*bottom*) distributions at the wall for different inlet turbulence intensities

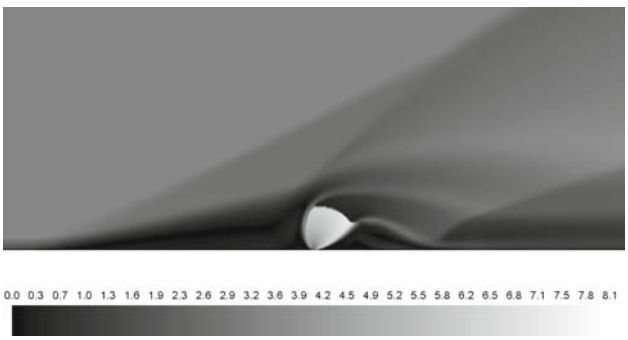

Fig. 14 Mach number contours for case 7

at 41.15 mm and for 0.05 and 0.005% of TI it takes place at 55.37 mm, compatible with experimental findings. Therefore a TI of 0.05% is selected as the inlet turbulence intensity.

Finally, a computational grid of 397 × 190 on a domain of 365.6 mm × 100 mm with inlet TI of 0.05% and jet TI of 2.5% is adapted for the rest of the numerical simulations. Figures 14 and 15 present Mach number contours and streamlines at the proximity of the injection location for

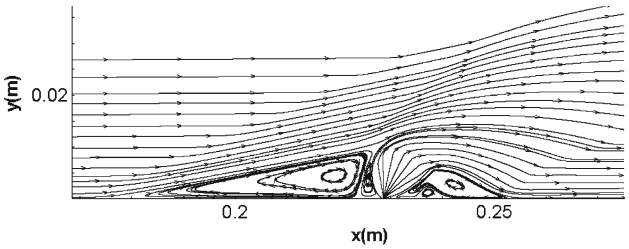

Fig. 15 Streamlines around the jet injection port for case 7

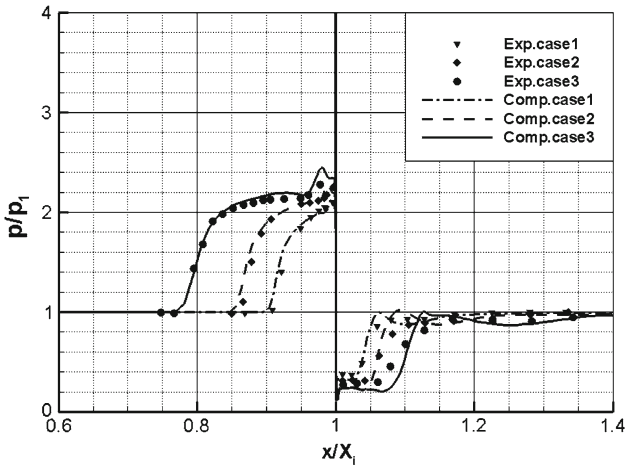

Fig. 16 Comparison of non-dimensional wall pressure distributions for cases 1–3

case 7 with this grid and these turbulence intensity values. All the upstream and downstream circulation flow structures are resolved clearly. Mach disc is captured in detail as well. Incoming flow changes its direction and becomes parallel to the sonic surface on top of PUV and PDV via a separation shock. Then another change in direction occurs around above the Mach disc via a jet induced bow shock; streamlines become curved. Consequently, incoming free stream moves over the injection plume. Finally, curved streamlines that are passing over PDV and SDV are diverted parallel to the wall via a recompression shock at the downstream of PDV. The extents of separated regions and jet penetration height are strongly dependent on the state of the approaching boundary layer and jet to free stream momentum flux ratio, J, as noted by Dhinagaran and Bose [11].

5.1.2 Wall pressure distributions

Figures 16 and 17 represent the comparison of computed non-dimensional wall pressure distribution with experimental data of Spaid et al. [1] for cases 1–3 and cases 4–7. Computed non-dimensional wall pressure distributions show good agreement with experimental data in all cases for all pressure ratios on the contrary to findings from other authors referenced. The extents of the separation regions in cases 1–3

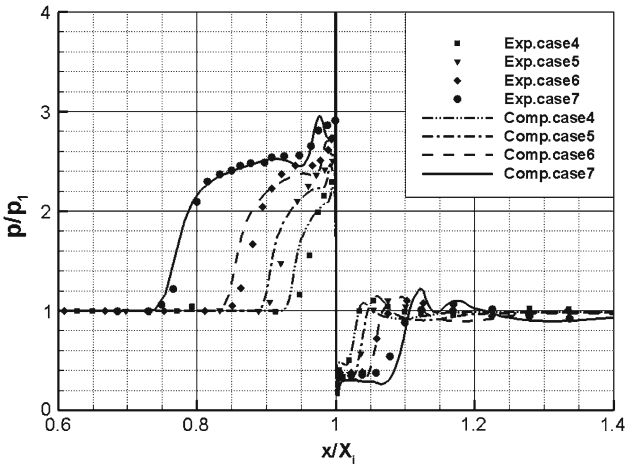

Fig. 17 Comparison of non-dimensional wall pressure distributions for cases 4–7

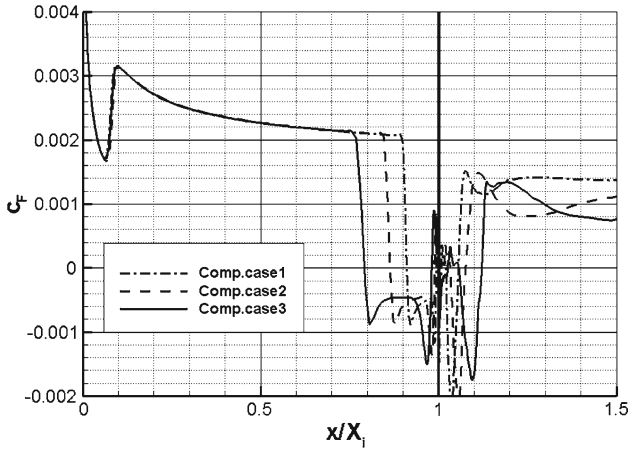

Fig. 18 Skin friction coefficient distributions for cases 1–3

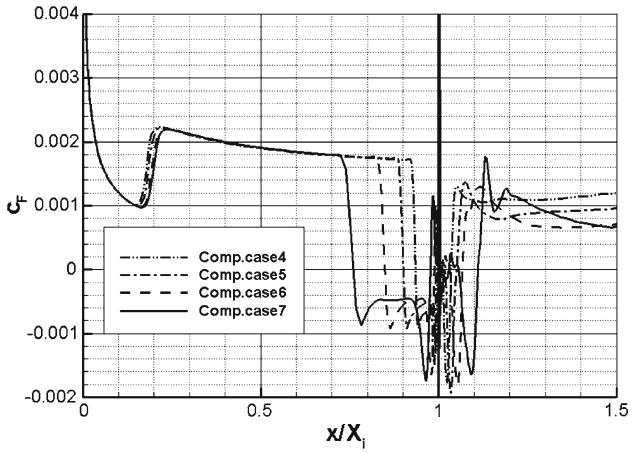

Fig. 19 Skin friction coefficient distributions for cases 4–7

are estimated quite accurately and for cases 4–7 they are predicted within 5% error. The slope of the pressure rise before plateau is predicted very closely to the experimental values for cases 1–3 and within a small error margin for cases 4–7. The magnitude of the pressure spike (region 3) for all cases is found accurately. Although previous studies from Chenault and Beran [12], Sriram and Mathew [16] predicted steeper upstream pressure rises and more accurate separation lengths for cases 4–5, they significantly underpredicted pressure spike at especially high pressure ratios (cases 6–7). Nevertheless, the authors predict not only the upstream pressure rise, the separation length accurately for cases 1–3 and within good accuracy range for cases 4–7, but also the magnitude of pressure spikes that are very accurately estimated for all cases as well. At the downstream side the length of the pressure well (region 4) is predicted closely to the experimental results except for cases 3 and 7 (high pressure ratio cases) where there is a little discrepancy, which is acceptable. As expected, as the pressure ratio increases (thus J), transverse jet penetrates further into the main stream, upstream and downstream circulation regions extend further upstream and downstream, respectively, and the pressure plateau and subsequent pressure rise become clearer.

5.1.3 Skin friction coefficient distributions

Skin friction coefficient is plotted in Figs. 18 and 19 that specify the extent of the upstream separation zones and the approximate location for transition to turbulence. Transition locations are found to comply fairly well with experimental findings.

For cases 1–3 laminar boundary layer undergoes transition about 21.72–23.77 mm from the tip of the plate, which is underpredicted, whereas for cases 4–7 it is found to be between 49.15 and 55.32 mm, which is well predicted. Considering the fact that experimental transition locations were determined using schlieren/ shadowgraph photography techniques, they inherently include uncertainty due to old film recording techniques, in addition the other factors such as bluntness, roughness, acoustic radiation from wind tunnel walls can significantly affect transition, which were not reported in data set. On the numerical side the uncertainty in turbulence modelling plays a major role in capturing transition as RANS/FANS models depend on the modelling of whole range of the scales of turbulence rather than resolving. Moreover, they employ Boussinesq hypothesis that assumes eddy viscosity is an isotropic scalar quantity, which is not necessarily true for many flowfields involving secondary flows. Thus, the simulated range of transition locations is acceptable.

Table 3 summarizes upstream flow conditions with Mach disc height or plume height, h, and transition and separation locations non-dimensionalised by injection location for all cases.

Table 3 Upstream flow conditions, Mach disc height and non-dimensional transition locations and separation lengths

Case	M_1	p_1 (mbar)	δ (mm)	h (mm)	$\frac{x_{tr}}{X_i}$	$\frac{x_{sep}}{X_i}$
1	2.6	67.09	2.91	3.30	0.095	0.089
2	2.6	66.29	2.76	5.90	0.099	0.136
3	2.6	66.88	2.51	10.0	0.104	0.209
4	3.48	32.35	2.91	1.93	0.215	0.065
5	3.48	32.44	2.76	3.50	0.224	0.99
6	3.48	32.47	2.55	5.90	0.233	0.15
7	3.48	32.50	2.28	10.0	0.242	0.239

5.1.4 Jet penetration and separation region

For jet penetration, Mach disc height non-dimensionalised by undisturbed boundary layer thickness just at the upstream of separation region, h/δ, is plotted against momentum flux ratio, J for all cases in Fig. 20. Almost perfectly linear fits are applied and equations with R^2 values (a measure of how good the fit is; 1 for perfect fit), are shown. h/δ is particularly important in scramjet applications as it represents the ability of fuel to penetrate over the boundary layer and mix with denser air rather high-temperature low-density flow near the wall. The trends show that as the momentum flux ratio is increased higher penetration into the main crossing flow is observed. For the same J value, cases 4–7 ($M_1 = 3.48$) provide deeper penetration compared with cases 1–3 ($M_1 = 2.6$). This can be explained by the increased jet pressure ratio having the same J value.

In case of the extent of separation region, separation location, x_{sep}, is plotted against Mach disc height in Fig. 21 for all cases. Perfectly linear fits are again applied with equations and R^2 values. Separation location is found to be a linear function of plume height and as the jet pressure ratio is increased separation region extends upstream, which is observed naturally in the experiments as well. The slope of the fits are 4.93 and 4.09 for $M_1 = 3.48$ and $M_1 = 2.6$, respectively. Spaid and Zukoski [1] observed the separation region being around four times the plume height in their experiments. Therefore, above findings are also compatible with experimental observations.

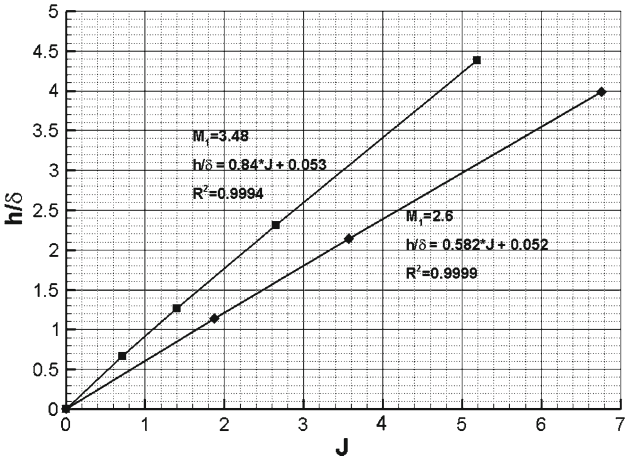

Fig. 20 Mach disc height non-dimensionalised by undisturbed boundary layer thickness versus momentum flux ratio

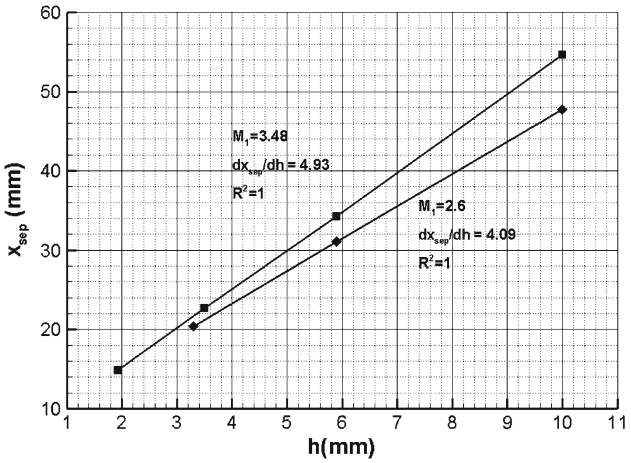

Fig. 21 Separation location versus Mach disc height

5.2 Experimental results-round jet injection case

5.2.1 Boundary layer on the flat plate and analytical estimates

The high-speed boundary layer developing on the flat plate within the achievable range unit Reynolds numbers is laminar unless tripped. To verify this fact an approach on transition by Simeonides [23] is employed. In his approach flat plate transition data from many different facilities are collected, and a unique way is proposed to correlate these data with characteristic parameters such as leading edge thickness, viscous interaction parameter, etc. Transition phenomenon is classified into two major categories: viscous dominated transition and bluntness dominated transition. The parameter defining this classification is simply the ratio of a bluntness parameter, β to viscous interaction parameter, $\bar{\chi}$ at the transition location. If it is greater than 1.9 it is bluntness-dominated transition; otherwise, it is viscous-dominated transition. When data are separated two very good correlation plots can be drawn, Re_{tr} against $Re/m/M$ for viscous-dominated transition, Mx_{tr}/b against Re_b/M^2 for bluntness-dominated transition, where b is leading edge thickness. Therefore, x_{tr} is estimated as 200 mm from the leading edge for the current sharp flat plate from the viscous-dominated transition plot. Considering the length of the plate being 155 mm, the incoming boundary layer is laminar.

Table 4 Experimental test conditions

Test no.	p_0 (mbar)	T_0 (°K)	$Re/m \times 10^6$	$p_{0_{jet}}$ (mbar)	J
1	6460	372	13.11	675	1.16
2	6490	375	13.0	1590	2.75
3	6390	374	12.81	3030	5.30
	±1%	±0.5%	±3%	±0.03%	±4%

Moreover, to further prove this point, experimental δ is measured from schlieren pictures utilising the fact that there is a significant density gradient along compressible boundary layers, gradually increasing away from the wall and becoming maximum at the boundary layer edge as noted by Smits and Dussage [22]. Needham [24] had shown that the outer edge of dark line in the schlieren pictures is very close to the boundary layer edge, and hence it can be taken as a measure of boundary layer thickness. Nevertheless, in the current configuration knife edge is positioned in a way that any gradient in positive y direction appears as a bright region; hence, the end of the bright line is taken as a reference. Thus, the boundary layer thickness is found to be 1.44 mm at 63 mm from the leading edge (just upstream of the separation region) for the Test 3 (see Table 4) from Fig. 22. The figure shows schlieren visualisation of the laminar boundary layer developing on the flat plate, in the presence of sonic turbulent transverse jet.

The result is compared with the analytical estimate from Popinski and Ehrlich [25], which reveals laminar boundary layer thickness for sharp leading edge flat plate as

$$\delta = \frac{5.2x}{\sqrt{\frac{p}{p_\infty} Re_x^*}} \quad \text{and} \quad \frac{Re_x^*}{x} = \frac{Re_x}{x}\left(\frac{T_\infty}{T^*}\right)^{1.76} \tag{13}$$

where Re_x^* is computed at reference temperature, T^*, which is calculated by Eckert's method [26].

The pressure variation along the flat plate in the above equation, i.e., p/p_∞ is governed by viscous interaction phenomenon explained in Sect. 2, and the parameter for this interaction is expressed below in (14).

$$\bar{\chi} = M_\infty^3 \sqrt{\frac{C_w}{Re_x}} \tag{14}$$

where C_w is Chapman Rubesin constant at the wall and defined in (15). T_e and μ_e are temperature and dynamic viscosity at the boundary layer edge, respectively. The subscript w represents wall values.

$$C_\mathrm{w} = \frac{\rho_\mathrm{w}\mu_\mathrm{w}}{\rho_\mathrm{e}\mu_\mathrm{e}} \approx \left(\frac{T_\mathrm{w}}{T_\mathrm{e}}\right)^{-1/3} \tag{15}$$

If $\bar{\chi}$ is small, less than 3, weak interaction occurs if it is greater than three strong interaction dominates. For the current tests only weak interaction is attainable; therefore, following formulas for both an insulated and a cold flat plate by Anderson [27] are employed.

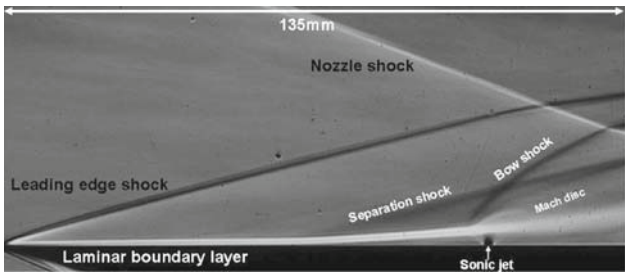

Fig. 22 Schlieren visualisation of the flowfield in the presence of the sonic transverse jet

For an insulated plate ($T_\mathrm{w} \approx T_\mathrm{aw}$)

$$\frac{p_\mathrm{e}}{p_\infty} = 1 + 0.31\bar{\chi} + 0.05\bar{\chi}^2 \tag{16}$$

For a cold plate ($T_\mathrm{w} < T_\mathrm{aw}$)

$$\frac{p_\mathrm{e}}{p_\infty} = 1 + 0.078\bar{\chi} \tag{17}$$

T_w is the wall temperature and T_aw, is the adiabatic wall temperature, i.e., the temperature at the wall when the flow is decelerated to zero velocity adiabatically. However, due to viscous dissipation some of the flow enthalpy is dissipated in the boundary layer. In fact, compressible boundary layers are neither adiabatic nor isentropic; a thermal boundary layer forms even in the presence of adiabatic conditions as noted by Schlichting [28]. Therefore, the adiabatic wall temperature is obtained by correcting the stagnation temperature outside the boundary layer with a recovery factor, r, as shown in (18).

$$T_\mathrm{aw} = T_\mathrm{e}\left(1 + r\frac{\gamma - 1}{2}M^2\right) \tag{18}$$

The recovery factor is strongly related to Prandtl number, Pr, and equal to $\sqrt{Pr}$ for laminar flows and $r = \sqrt[3]{Pr}$ for turbulent flows.

Finally, the estimate from Popinski and Ehrlich gives δ as 1.18 mm at 63 mm from the leading edge, which is smaller than 1.44 mm measured. The discrepancy can be attributed to the presence of tappings disturbing the boundary layer flow slightly via creating weak Mach waves and heat transfer during the test time of 5 seconds that increases wall temperature which implicitly affects reference temperature.

From Fig. 22, the following flow structures can also be seen: a curved leading edge shock due to viscous interaction at the leading edge and following laminar boundary layer growth up to the separation point accompanied by diversion in upward direction thereafter. Separation shock emanates around the separation point and intersects the jet induced

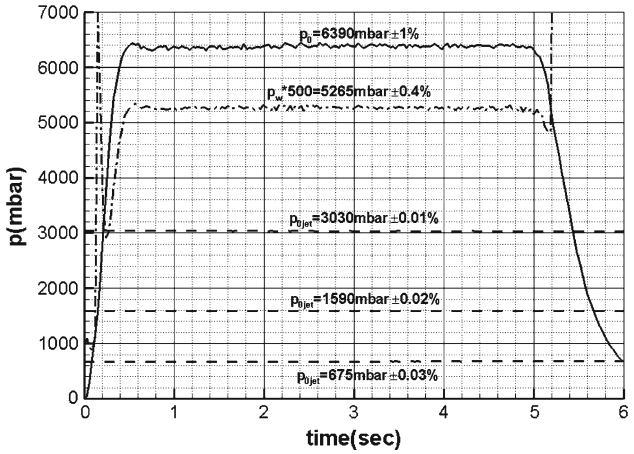

Fig. 23 Time histories of tunnel and jet stagnation pressure signals with a representative wall static pressure signal

bow shock; sonic jet expands suddenly and aligns itself backwards; afterwards, it is terminated by Mach disc. Separation region, separation shock and bow shock are three-dimensional curved flow structures around the transverse jet as opposed to two-dimensional slot injection. Finally, the nozzle shock is reflected after crossing leading edge shock and bow shock.

5.2.2 Round jet injection into mach 5 crossflow

In the tests sonic turbulent jet is regulated to give $Re_{D\text{jet}}$ values of 1.97, 4.64 and 8.84 $\times$ 10^4 and started just before the test. The experimental test conditions are tabulated in Table 4. Figure 23 shows the time histories of tunnel stagnation pressure, p_0 for test 3, jet stagnation pressure, $p_{0\text{jet}}$ for tests 1–3 and wall pressure, p_w at the first tapping in the centre again for test 3. Also the variations of the pressure values are depicted proving steady conditions prevailed during the tests.

However, the interaction of the transverse jet with the incoming flow is unsteady owing to jet shear layer instabilities coupled with incoming boundary layer. In the region near the injector exit, the injectant fluid moves with a higher velocity tangent to the interface than the incoming flow. As a result, large vortices are periodically formed, engulfing large quantities of free stream fluid and drawing it into the jet shear layer, and then are convected downstream at high speeds. Therefore, bow shock is affected by these vortices and is oscillatory in nature. Furthermore, separation shock is unsteady as well due to the disturbances in the injection vicinity that are fed upstream through the boundary layer. Nevertheless, within the scope of this article only steady features of jet interaction are considered.

The mean values of pressure signals, $\overline{p}$, during the useful running time are calculated using the equation below.

$$\overline{p} = \frac{1}{t_f - t_i} \int_{t_i}^{t_f} p(t)\mathrm{d}t$$

Figure 24 represents non-dimensional wall pressure distributions for tests 1–3 both at $z = 0$ mm line and the $z = -20$ mm line. In addition, the estimates for wall pressure distribution using weak viscous interaction formulas (16, 17) are drawn as well. These estimates show good correlation with first experimental data point at 25 mm from the leading edge; in terms of trends, weak viscous interaction formula for an adiabatic plate results in a slightly better behaviour. However, considering the experimental uncertainty in pressure measurements is within 5% error band, both formulas are acceptable. Moreover, the symmetry of the incoming flow field is ensured at first three tappings by checking values at the centre ($z = 0$) and off centre ($z = 20$ mm and $z = -20$ mm). The pressure rise due to the injection does not become apparent until a x/X_i value of 0.5 for test 3 and until 0.75 for tests 1, 2; afterwards, it rises gradually implying laminar separation for all tests. Downstream of the injection the low-pressure well is apparent which is accompanied by recompression shock. The amplitudes of the upstream and downstream regions tend to increase with increasing jet pressure, thus increasing momentum flux ratio as expected. In case of lateral spreading a similar conclusion can be made; as the jet stagnation pressure hence the momentum flux ratio, J, is increased a bigger region is affected by the jet laterally in both upstream and downstream directions.

5.2.3 Jet penetration and separation region

Transverse jet penetrates further for higher values of J; curved bow shock moves away from the surface and curved separation region extends in both upstream and downstream directions as deducted from Fig. 25. The three-dimensionality of the flow structures is superimposed on schlieren images as expected. Curved recompression shock occurs just above the separation region downstream of the jet. These observations are compatible with the findings reported in the literature. Mach disc height and the extent of the separation region can be extracted from schlieren images using digital image processing that is employed before to find incoming boundary layer thickness just at the upstream of the separation region. These values are tabulated in Table 5.

Mach disc height non-dimensionalised by undisturbed boundary layer thickness just at the upstream of separation region, h/δ, is plotted against momentum flux ratio, J in Figs. 26, 27. This time, almost perfectly power law fit is applied and equation with R^2 value is shown. The penetration increases with increasing momentum flux ratio; however,

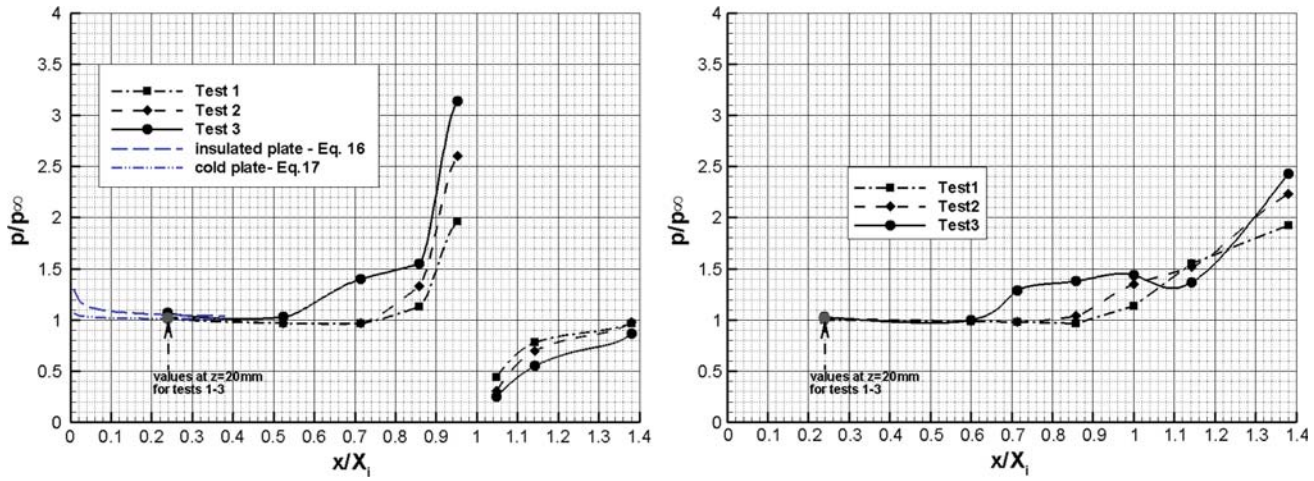

Fig. 24 Non-dimensional wall pressure distributions for tests 1–3; *top* $z = 0$ mm, *bottom* $z = -20$ mm

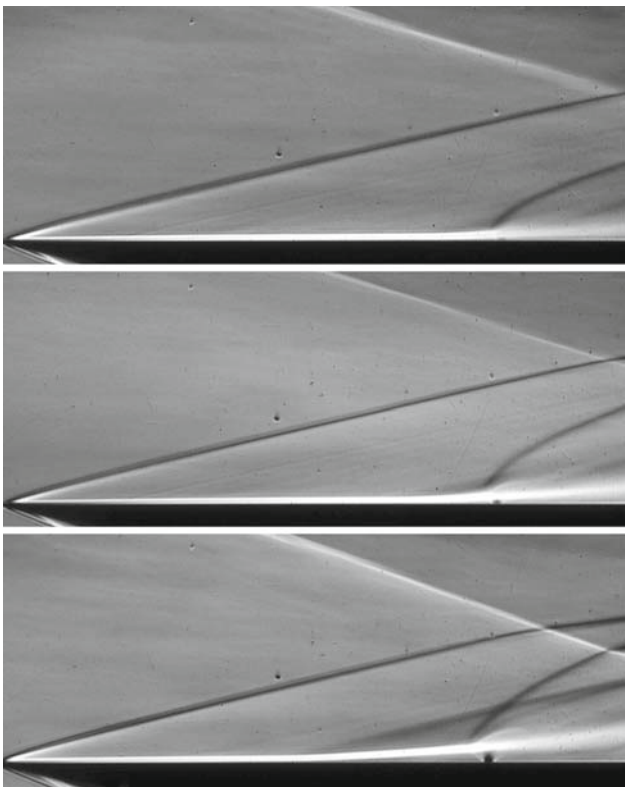

Fig. 25 Schlieren visualisation of flowfield in the presence of the sonic transverse jet; *top* test 1, *middle* test 2, *bottom* test3

Table 5 Experimental boundary layer thicknesses, Mach disc heights and non-dimensional separation lengths

Test No	δ (mm)	h (mm)	x_{sep}/X_i
1	1.34	3.28	0.125
2	1.38	5.19	0.238
3	1.44	7.81	0.4

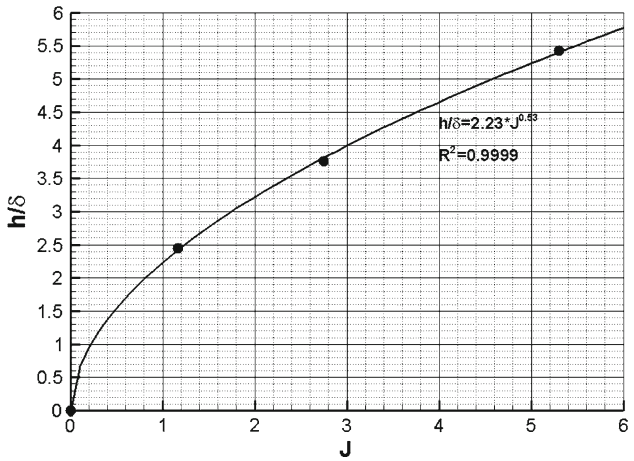

Fig. 26 Experimental Mach disc height non-dimensionalised by undisturbed boundary layer thickness versus momentum flux ratio

trend is nonlinear in this case. This finding is consistent with the results obtained by Papamoschou and Hubbard [7]. Their results show that sonic/supersonic penetration through a circular hole into high-speed crossflow is not dramatically different than a subsonic power law fit when penetration over jet diameter is drawn against momentum flux ratio. In case of separation location against Mach disc height, a linear fit is obtained and the slope of the fit is around 6.4 as shown in Fig. 27. The extent of the separation region is strongly governed by the state of the incoming boundary layer as the bow shock induces adverse pressure gradient and causes it to separate. Generally, for three-dimensional jet interactions the separation region is closer to the injection port due to three-dimensional relieving effect, but in this case the boundary layer is laminar, and thus it is less resistant to adverse pressure gradients, and it separates earlier than a turbulent boundary layer.

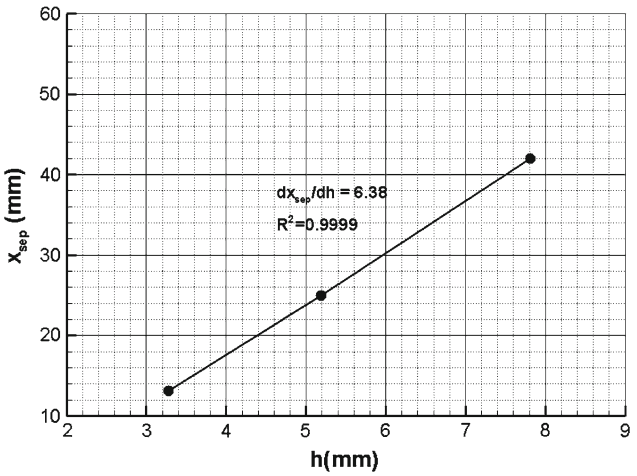

Fig. 27 Experimental separation location versus Mach disc height

6 Conclusion

The present investigation aimed mainly to improve numerical simulations to match experimental data of Spaid and Zukoski [1] for a wider range of pressure ratios, including capturing transition locations, and to study the effect of incoming flow and jet turbulence levels on jet interaction phenomenon. This set of experiments is of greater value because of good spatial resolution around the injection port. Sidewalls ensured two-dimensionality and the cases where three-dimensional effects started to appear were clearly documented. In addition, the range of injection pressure ratio is large. The upstream pressure rise was steep, implying separation of a turbulent boundary layer after undergoing transition at 50.8–76.2 mm from the leading edge of the plate. Computed non-dimensional wall pressure distributions showed very good agreement with experimental data for cases 1–3 and good agreement for cases 4–7. In addition, transition locations were captured with acceptable accuracy. As the jet pressure ratio is increased, prominent flow structures extend further in upstream and downstream directions. Jet penetration is found to be a linear function of momentum flux, and the separation location extends upstream about four times the penetration height. The results are found to be insensitive to jet turbulence intensity; however, transition location is strongly influenced by inlet turbulent intensity. $\kappa - \omega$ SST model provided quite accurate results over a wide range of pressure ratios for such a complex flow field.

To complement numerical simulations, few experiments involving a sonic round jet injected on a flat plate into high-speed cross flow at Mach 5 were carried out. The effect of pressure ratio on three-dimensional jet interaction dynamics was examined. The incoming boundary layer was laminar. As the jet pressure ratio is increased, prominent curved flow structures extend in spanwise direction as well as in upstream and downstream directions. Jet penetration is found to be a non-linear function of momentum flux for three-dimensional jet interactions, and the separation location extends upstream about six times the penetration height. Three-dimensional numerical simulations to compare against experiment results of authors are in progress.

References

1. Spaid, F.W., Zukoski, E.E.: Study of the interaction of gaseous jets from transverse slots with supersonic external flows. AIAA J. **6**(2), 205–212 (1968)
2. Spaid, F.W.: Two-dimensional jet interaction studies at large values of Reynolds and Mach numbers. AIAA J. **13**(11), 1430–1434 (1974)
3. Schetz, J.A., Billig, F.S.: Penetration of gaseous jets injected into a supersonic stream. J. Spacecr. Rockets **3**(11), 1658–1665 (1966)
4. Parthasarathy, K., Zakkay, V.: An experimental investigation of turbulent slot injection at Mach 6. AIAA J. **8**(7), 1302–1307 (1969)
5. Hawk, N.E., Amick, J.L.: Two-dimensional secondary jet interaction with a supersonic stream. AIAA J. **5**(4), 555–660 (1967)
6. Werle, M.J., Driftmyer, R.T., Shaffer, D.G.: Jet-interaction-induced separation: the two-dimensional problem. AIAA J. **10**(2), 188–193 (1971)
7. Papamoschou, D., Hubbard, D.G.: Visual observations of supersonic transverse jets. Exp. Fluids **14**, 468–476 (1993)
8. Kumar, D., Stollery, J.L., Smith, A.J.: Hypersonic jet control effectiveness. J. Shock Waves **7**, 1–12 (1997)
9. Kontis, K., Stollery, J.L.: Control effectiveness of a jet-slender body combination at hypersonic speeds. J. Spacecr. Rockets **34**(6), 762–768 (1997)
10. Rizzetta, D.P.: Numerical simulation of slot injection into a turbulent supersonic stream. AIAA J. **30**(10), 2434–2439 (1992)
11. Dhinagaran, R., Bose, T.K.: Numerical simulation of two-dimensional transverse gas injection into supersonic external flows. AIAA J. **36**(3), 485–487 (1998)
12. Chenault, C., Beran, P.S.: $\kappa - \epsilon$ and Reynolds stress turbulence model comparisons for two-dimensional flows. AIAA J. **36**(8), 1401–1412 (1998)
13. Qin, N., Redlich, A.: Massively separated flows due to transverse sonic jet in laminar hypersonic stream. J. Shock Waves **9**, 87–93 (1999)
14. Srinivasan, R., Bowersox, R.D.W.: Assessment of RANS and DES turbulence models for supersonic jet interaction flows. AIAA Paper 2005-499 (2005)
15. Won, S., Jeung, I., Choi, J.Y.: DES study of transverse jet injection into supersonic cross flows. AIAA Paper 2006-1227 (2006)
16. Sriram, A.T., Mathew, J.: Improved prediction of plane transverse jets in supersonic crossflows. AIAA J. **44**(2), 405–408 (2006)
17. Gruber, M.R., Nejad, A.S., Chen, T.H., Dutton, J.C.: Mixing and penetration studies of sonic jets in a Mach 2 freestream. J. Propuls. Power **11**(2), 315–323 (1995)
18. Santiago, J.G., Dutton, J.C.: Crossflow vortices of a jet injected into a supersonic crossflow. AIAA J. **35**(5), 915–917 (1997)
19. Chenault, C.F., Beran, P.S., Bowersox, R.D.W.: Numerical investigation of supersonic injection using a Reynolds-stress turbulence model. AIAA J. **37**(10), 1257–1269 (1999)
20. Srinivasan, R., Bowersox, R.D.W.: Characterization of flow structures and turbulence in hypersonic jet interaction flowfields. AIAA 2005-0895
21. Fluent v.6.3.26 Documentation (2006)

22. Smits, J.A., Dussage, J.P.: Turbulent shear layers in supersonic flow. Springer, New York (2006)
23. Simeonides, G.A.: Correlation of laminar-turbulent transition data over flat plates in supersonic/hypersonic flow including leading edge bluntness effects. J. Shock Waves **12**, 497–508 (2003)
24. Needham, D.A.: Laminar separation in hypersonic flows. PhD thesis, University of London, (1965)
25. Popinski, Z., Ehrlich, C.F.: Development design methods for predicting hypersonic aerodynamic control characteristics. AFFDL-TR-66-85, (1966)
26. Eckert, E.R.G.: Engineering relations for friction and heat transfer to surfaces in high velocity flow. J. Aeronaut. Sci. **22**, 585–587 (1955)
27. Anderson, J.D. Jr.: Hypersonic and high-temperature gas dynamics. McGraw-Hill, New York (2006)
28. Schlichting, H., Gersten, K.: Boundary layer theory. Springer, Berlin (2001)